Microphysical view of development and ice production of mid-latitude stratiform clouds with embedded convection during an extratropical cyclone

Yuanmou Du[1,3], Dantong Liu[2], Delong Zhao[1,3], Mengyu Huang[1,3], Ping Tian[1,3], Dian Wen[1,3], Wei Xiao[1,3], Wei Zhou[1,3], Hui He[1,3], Baiwan Pan[2], Dongfei Zuo[4], Xiange Liu[1,3], Yingying Jing[1,3], Rong Zhang[4], Jiujiang Sheng[1,3], Fei Wang[1,3], Yu Huang[1,3], Yunbo Chen[1,3], Deping Ding[1,3]

[1]Beijing Weather Modification Center, Beijing, 100089, China
[2]Department of Atmospheric Sciences, School of Earth Sciences, Zhejiang University, Hangzhou, Zhejiang, 310027, China
[3]Beijing Key Laboratory of Cloud, Precipitation and Atmospheric Water Resources, Beijing, 100089, China
[4]CMA Weather Modification Center, Beijing, 100081, China

Correspondence to: dantongliu@zju.edu.cn

Abstract. The microphysical properties associated with the ice production importantly determine the precipitation rate of clouds. In this study, the microphysical properties including the size distribution and particle morphology of water and ice for stratiform clouds with embedded convection during an extratropical cyclone over the northern China were in-situ characterized. Stages of cloud were investigated including young cells rich of liquid water, developing and mature stages with high number concentration of ice particles（N_{Ice}）. The N_{Ice} could reach 300 L^{-1} at the mature stage, about two orders of magnitudes higher than the primary ice number concentration calculated from ice nucleation. This high N_{Ice} occurred at about −5 to −12 ºC, spanning the temperature region of Hallett-Mossop process and possible other mechanisms for the secondary ice production (SIP). The N_{Ice} was positively associated with the number concentrations of graupel with diameter (d) > 250 μm and large supercooled droplet (d > 50 μm). The SIP rate was 0.005-1.8 $\text{L}^{-1}\text{s}^{-1}$ derived from the measured N_{Ice} with known ice growth rate between two sizes. The SIP rate could be produced by a simplified collision-coalescence model within an uncertainty factor of 5, by considering the collection of large droplets by graupel. The collection efficiency between the graupel and droplet was found to increase when the size of droplet was closer to graupel which may improve the agreement between measurement and model. Importantly, the overall N_{Ice} was found to be highly related to the distance to cloud-top (DCT). The level with larger DCT had more abundant rimmed graupels falling from the above level, which promoted the coalescence processes between graupels and droplets, producing a higher fraction of smaller ice through SIP. This seeder-feeder process extended the avalanche SIP at lower temperature up to −14 ºC beyond the temperature region of Hallett-Mossop process. The results illustrated the microphysical properties of clouds with convective cells under different stages, which will improve the understanding of the key processes in controlling the cloud glaciation and precipitation process.

1 Introduction

The mid-latitude clouds are mostly present in mixed-phase (Mülmenstädt et al., 2015). The microphysical properties associated with the ice production or the conversion from liquid water to ice importantly determine the precipitation rate and lifetime of clouds (Lau and Wu, 2003; Cantrell and Heymsfield, 2005). The growth rate of hydrometeors through the ice phase is usually more rapid than the warm rain process (Lohmann and Feichter, 2005; Mcfarquhar et al., 2017). Understanding the ice production and glaciation process in clouds is important for more accurate parameterization of microphysical processes in weather prediction models (Korolev et al., 2017; Bacer et al., 2021), and this needs to be understood in vertical dimension and under different stages of cloud development (Zhao et al., 2019) .

In addition to the primary ice produced by homogeneous and heterogeneous nucleation processes from aerosol particles (Kanji et al., 2017), the secondary ice production (SIP) process can rapidly produce high numbers of ice up to several orders of magnitude more than that produced from ice nucleation (Mossop, 1985; Harris-Hobbs and Cooper, 1987; Field et al., 2016; Korolev et al., 2022), which is an important process to accelerate the cloud glaciation. The SIP can occur under different ambient temperatures through different processes including the rime splintering process, fragmentation during droplet freezing, fragmentation due to ice–ice collision, ice particle fragmentation due to thermal shock, fragmentation of sublimating ice particle, and the activation of ice-nucleating particles in transient supersaturation around freezing drops (Korolev et al., 2020). The Hallett-Mossop (H-M) mechanism was well reproduced through laboratory work (Hallett and Mossop, 1974) and is usually introduced to explain the high abundance of ice number concentration at slightly sub-freezing temperature (−3 to −8 °C) (Hogan et al., 2002; Huang et al., 2008; Crosier et al., 2013; Korolev et al., 2022), and the freshly formed ice mostly exhibited the shapes of columns or needles (Locatelli et al., 2008; Crosier et al., 2011; Lloyd et al., 2014; Taylor et al., 2016), consistent with the diffusion growth habit of ice under such temperature. However, the H-M process may not sufficiently explain the even more rapid SIP rate in observation, the fragmentation during droplet freezing and ice-ice collision may play an important role in the secondary ice production process (Rangno and Hobbs, 2001), it may also be formed by the growth of ice from the outside into the H-M temperature zone (Field et al., 2016). Supercooled large drop may play important roles in the SIP process, which can fracture when freezing and emit ice splinters (Lawson et al., 2015), and this process could extend the SIP to a lower temperature under the influence of strong updraft. A recent study also found SIP process could occur at temperature as low as −27 °C (Korolev et al., 2022).

Mid-latitude clouds formed from extratropical cyclone are the main sources of precipitations for the east Asia (Li et al., 2016). The microphysical properties of clouds over the North China Plain have been observed during frontal systems (Yang et al., 2017; Hou et al., 2021; Hou et al., 2023). It was found more ice particles close to the convective region and the SIP was found to produce ice number concentration up to over 300 L^{-1}, which may promote the intensity of precipitation. These studies suggest that the SIP process may be explained by the H-M process or other mechanisms, such as collisional fragmentation, which may contribute to SIP in regions that do not fit the H-M criteria (Hou et al., 2023). However, the key factors in controlling the SIP process and how these factors can influence the SIP at different stages of clouds have not been elucidated.

The cold front system formed by the merging of cold air from the rear of extratropical cyclones with the warm air mass brought in by the southwest warm and moist air along the edge of the subtropical high-pressure system is the main weather system that produces rainfall in northern China (Wang et al., 2014). This study therefore investigated the microphysical properties of mid-latitude cloud formed via this typical weather system over the North China Plain through aircraft in-situ measurements. Stages of cloud were investigated including young cells rich of liquid water, developing and mature stages with high number concentration of ice particles. The key factors in controlling SIP are elucidated through the calculation from measurements and modelling.

2 Experiment

2.1 Instrumentation

The Kingair350 aircraft of Beijing weather modification center was employed for in-situ measurements in this experiment (Liu et al., 2020; Tian et al., 2020; Zuo et al., 2023). This experiment aimed to conduct continuous aircraft observations of clouds developed during an extratropical cyclone over northern China. The goals were to obtain in-situ microphysical data of clouds during the development of frontal system and to study the production of ice in clouds. The experiment was designed based on numerical model forecasting results and real-time radar data. To capture the microphysical characteristics of stratiform clouds with embedded convection at various development stages, aircraft observational experiment was conducted in accordance with real-time changes in precipitation radar echoes.

The air temperature was measured by Rosemount total-air temperature probe (Lenschow and Pennell, 1974; Lawson and Cooper, 1990). The temperature may be underestimated due to water evaporation however this artifact is negligible for supercooled clouds (Lawson and Rodi, 1992; Korolev and Isaac, 2006), and the temperature shift in and out of clouds was not observed in this study. The wind speed and wind direction were measured by Aircraft Integrated Meteorological Measurement System (AIMMS20, Aventech Research Inc.) with a time resolution of 1 second (Beswick et al., 2008). The distribution of aerosol particles ranging from 0.1 to 3 μm in diameter was measured by Passive Cavity Aerosol Spectrometer Probe (PCASP, DMT Inc.) with a time resolution of 1 second (Cai et al., 2013).

The Fast Cloud Droplet Probe (FCDP, SPEC inc.) (Lance et al., 2010) was used to measure cloud droplets with a diameter range of 2-50 μm and a resolution of about 3 μm. It resolves the particles into 20 size bins, and the optical sizing was calibrated with known-sized standard glass beads. The liquid water content (LWC) at diameter of 2-50 μm was calculated by integrating the volume at all size bins by the FCDP (Lu et al., 2012). Two-dimensional stereoscopic optical array imaging probe (2D-S, SPEC Inc.) was used to record images of cloud particles and provide the size, shape and concentration of particles. 2D-S has two orthogonal laser beams that cross in the middle of the sample volume and casts the shadowgraph of particles on two linear 128-photodiode arrays when the particles transit through the laser (Lawson et al., 2006). It can measure particles of 10-1280 μm in diameter with a resolution of 10 μm, and provide detailed information of different phase particles in cloud. The precipitation particle was measured by High Volume Precipitation Spectrometer (HVPS, SPEC Inc.) (Lawson et al., 1998), which is also an imaging array probe with a measure range and resolution of 150-19200 μm and 150 μm respectively. The laser beam of HVPS illuminates the imaging system, and records shadow images on the 128 elements linear photodiode array when particles pass through the sample volume. The S-band weather radar located in Beijing (Jiang and Liu, 2014) was used to help analyze the macroscopic characteristics of cloud, which can detect targets within a radius of 230 km with a time and radial spatial resolution of 6 minutes and 1 km, respectively. The distance from the radar to the observed cloud system in this study was approximately 50-200 km.

The Optical Array Shadow Imaging Software was used to process the raw data of 2D-S and HVPS, which can distinguish liquid drop and ice particle according to the circularity of particles (*C*) (Crosier et al., 2011). The *C* is calculated from Eq. (1):

$$C=\frac{P^2}{4\pi A}, \tag{1}$$

where P and A are the perimeter around the edge of the particle and total area of the particle respectively. The perfect sphere has circularity of 1, and the other shapes have larger circularity. Irregular particles with larger circularity are counted as ice particles because the shape of ice is unlikely to be round. Considering the poorly imaged or distorted large drops/drizzles may be counted as ice particles, the circularity threshold for ice particles (irregular class) is raised to 1.2. Calculated circularity values may also be less than 1 due to the presence of images composed of only a small number of pixels, so the low threshold for water drops (round class) is reduced to 0.9. In practical terms, particles with an area less than 20 pixels are classified as the small class because it is difficult to determine the shape with few pixels, and particles with an area more than 20 pixels are classified as round class ($0.9 \le C < 1.2$) or irregular class ($C \ge 1.2$). The round and irregular class are regarded as liquid drop and ice particle, respectively. The round class is large droplet with a diameter larger than 50 μm, and it was represented by large droplet in this study to distinguish from the cloud droplets (2-50 μm) measured by the FCDP.

The shapes of irregular ice particles were further clarified into five habit classes including linear, plate, irregular, aggregate and dendrite, according to the maximum dimension, width, linearity, circularity and density of particles (Zhang et al., 2021). The mass of ice was determined by particle shapes according to the approximate mass formulas for ice particles (Holroyd, 1987), and hereby the ice water content (IWC) was calculated. It should be noted that the error in calculating ice mass according to the mass-dimension relationship will increase when ice particle is larger and the shape has large irregularity to be classified (Crosier et al., 2013). The total water content (TWC) was obtained by adding the IWC calculated from the 2D-S (diameter 10-1280 μm) and LWC measured by the FCDP (diameter 2-50 μm).

The concentration of ice nucleating particles (INP) in study was calculated by the parameterization relationship (Demott et al., 2010), which is expressed as:

$$n_{\mathrm{IN},T_k}=a(273.16-T_k)^b(n_{\mathrm{aer},0.5})^{(c(273.16-T_k)+e)}, \tag{2}$$

Where $a = 0.0000594$, $b = 3.33$, $c = 0.0264$, $e = 0.0033$. n_{IN,T_k} is the number concentration of INP (L^{-1}), and T_k is the temperature of cloud in degrees Kelvin, and $n_{\mathrm{aer},0.5}$ is the number concentration of aerosol particles with diameter larger than 0.5 µm. In this study, the PCASP measurement was conducted below cloud base, and the in-cloud PCASP data was excluded for analysis due to cloud particle shattering on the inlet. Therefore, $n_{\mathrm{aer},0.5}$ measured by PCASP below cloud base was used for calculation.

2.2 Overview of experiment

On 26th September 2017, light precipitation occurred in North China under the influence of eastward moved upper trough. ERA5 reanalysis data at 08:00 BJT (UTC+8h) with a resolution of 0.25 degrees from European Centre for Medium-Range Weather Forecasts (ECMWF) showed there was a deep cold vortex system in the northwest of East Asia at 500 hPa (Fig. 1a), the bottom of which split into the shortwave trough and moved eastward, leading to a southward moved cold advection at the middle-level and conditional instability stratification (Fig. S1). Figure 1b showed the existence of a convergence zone at 850 hPa, where a cold front was located, and sufficient water vapor was transported through the prefrontal southerly wind. The abundance of water vapor and upward motion of air led to the generation of a series of stratiform clouds, and convective clouds also appeared under the condition of instability stratification.

The study region in this research was Zhangjiakou, Hebei Province (northwest of Beijing) and Beijing, and aircraft departed from the airport in northern Beijing at 09:54 BJT and flew to Zhangjiakou. The precipitation mainly occurred in Zhangjiakou and became weaker after 11:00 BJT on 26th September 2017, then the precipitation band gradually moved to Beijing, and weather stations observation data indicated the precipitation rate during this experiment were generally less than 1 mm/h. Figure S2 shows the movement of the surface cold front, i.e., the convergence zone of cold and warm air masses at the surface as determined by the temperature and wind shear measured by the ground sites. The center of the extratropical cyclone was located in Outer Manchuria (Fig. S3), and the surface cold front extended southwestward from the position of the extratropical cyclone to the experimental region, the experimental region was situated within the trailing end of the cold front cloud system, which extended southward from the extratropical cyclone cloud system. At 09:00 to 12:00 BJT, the surface cold front continued to move southeastward and lifted the warmer and moist air mass in front. The warm air mass ascended along the front, forming clouds and precipitation, and the aircraft observation area was situated behind the cold front. The aircraft sampled the clouds formed in this cyclonic system at this stage, i.e. behind the surface cold front line (Fig. S3) and for the newly formed, developing and matured clouds. This is the typical cloud system formed in this extratropical weather system over the northern China.

3 Results and discussion

3.1 Identifying stages of cloud development

Four relative stages during the lifecycle of clouds were identified during experiment, which corresponded to the developing (P1), mature (P2), dissipating (P3) and young cells (P4) in cloud system, according to the different glaciation extents of clouds. The ice mass fraction (F_{Ice}: IWC/TWC) was used to indicate the different development stages of clouds (Fig. 2), by considering a more mature cloud has a more glaciated fraction, for the discussions of cloud microphysics at different stages. Although the glaciation extents between P2 and P3 were similar, P3 showed a narrower cloud band (Fig. 3) and a lower cloud-top (Fig. 4) for dissipating cells compared to the mature clouds in P2. The cloud system was formed through the combined effects of dynamic forcing induced by the frontal uplift and the moisture transport provided by the prefrontal southerly air mass. Therefore, this study postulated that the continuous clouds within the cloud system had similar dynamic and thermodynamic properties. Previous studies also pointed out the exchangeability between temporospatial domains of cloud properties in the same cloud system, where properties and evolution of individual clouds were similar (Lensky and Rosenfeld, 2006; Yuan et al., 2010; Coopman et al., 2020). Aircraft performed flight altitudes of 3.2-5.7 km in P1, 5.2-5.8 km in P2, 4.9-5.2 km in P3 and 2.1-4.9 km in P4, temperature and AIMMS data indicated that the 0 ℃ layer was at about 3.4 km. The flight tracks mapping on the composite reflectivity of precipitation radar are shown in Fig. 3, colored by the LWC from FCDP and IWC from 2D-S respectively, the radar times and the flight time windows for the four stages are shown in Table S1. In developing cells, substantial LWC was detected up to 0.3 g m^{-3}, and the aircraft penetrated a high IWC region in this cloud at 10:09-10:11 BJT, with the highest IWC exceeded 2 g m^{-3} (Fig. 3a1, b1), and F_{Ice} at this stage could span from zero (pure water) to unit (pure ice) (Fig. 2). In mature cells, F_{Ice} ranged in 0.36-1 and IWC generally exceeded 0.3 g m^{-3} (Figs. 2 and 3b2), and the maximum radar reflectivity of mature cells was enhanced from 20 dBZ to 27 dBZ at 10:06 to 10:42 BJT (Fig. 3a1, a2). At the dissipating stage, the ice phase precipitation process occurred and the radar reflectivity became weaker with narrowed cloud band (Fig. 3a3, b3), and the range of F_{Ice} reached up to 0.56-1 (Fig. 2). The last stage was young cells with lower glaciated fraction (Fig. 2), the rich liquid water produced from the newly developed thermals after the front cloud bands dissipated (Fig. 3a4, b4).

Figure 4 shows the microphysical properties of clouds and meteorological parameters along the flight track at four stages. The vertical wind data during aircraft turns were excluded from Fig. 4 and were not used for the analysis. The cross section of radar reflectivity in Fig. 4a can provide information about the relative positions of aircraft with respect to the cloud top and base, as well as the echo intensity of the cloud. The cross section of radar reflectivity along the flight track was calculated based on the aircraft position. A vertical line was first determined according to the latitude and longitude of the aircraft, then the azimuth angles, elevation angles, and range bins of equidistant points with a resolution of 30 m in the vertical line were obtained, and the radar reflectivity of each equidistant point was calculated by linear interpolation in nearest neighbor combined with a vertical direction (NVI) method. Hereby the radar profile with vertical resolution of 30 m along flight track was obtained. The cloud-top height is indicated by red line on the radar profile, where the areas with radar reflectivity factor more than or equal to 5 dBZ were considered as cloud, and other areas were considered as clutter. This might give a lower estimation for the height of cloud-top because the rain radar was only sensitive to clouds with precipitation, but might not efficiently detect clouds dominated by liquid water. The size spectrum of ice showed a bimodal mode with a minima diameter (d) at 180 μm (Fig. S4). The fraction of smaller ice with $d < 180$ μm ($F_{\text{smaller ice}}$) was defined to imply the freshly formed smaller ice which had not experienced sufficient growth (Fig. 4b). The sensitivity was tested by altering the threshold from 160-200 μm, and the resultant difference of smaller ice fraction was within 10%.

P1 featured strong updraft with vertical wind speed up to 8.9 m/s, and the strong updraft region was dominated by ice particles and precipitation particles (Fig. 4c-e). The low LWC when high vertical updraft may be caused by the rapid production of ice particles, which was also observed in tropical highly convective region (Lawson et al., 2015). The ice number peaked at a valley between two peaks of liquid water, but it was difficult to determine the vertical wind at the peak of ice number due to aircraft turns (Fig. 4). However, in the subsequent level flight, high ice number concentration (> 170 L^{-1}) was also observed in the strong updraft region. After the high ice number region, LWC up to 0.28 g m^{-3} was observed in the region with weaker updraft.

The cloud-top height in P2 reached 10 km (Fig. 4a), which was the highest cloud-top of clouds observed during experiment. The LWC in P2 was considerably lower compared to P1, while there were more large droplets and ice particles in clouds (Fig. 4d, e), and the distribution of large droplets and ice particles in P2 showed a bimodal distribution. The updraft strength in P2 was weaker than P1 (Fig. 4c), but P2 was more glaciated than P1 with F_{Ice} spanning from 0.36 to 1 (Fig. 2). P3 and P4 were relatively quiescent compared to other stages. The cloud-top height in P3 was lower than P2, and the area of stronger echoes (>20 dBZ) was also reduced compared to P2 (Fig. 4a). Similar to P2, the dissipating stage was dominated by ice but only intermittent unglaciated LWC-rich clouds were present (Fig. 4d, e), however, the clouds in P3 had a more glaciated fraction (Fig. 2). All above confirmed the dissipating stage of P3. P4 was likely a newly developed cell with lower F_{Ice} and weak radar reflectivity, and the cloud-top had not reached as high as other stages (Figs. 2 and 4a). This stage was rich of liquid water with LWC up to 0.27 g m^{-3} at a colder temperature (−11 ºC), while the IWC measured in the region was significantly lower compared to other stages (Figs. 4d, e and 5).

Figure 5 summarizes the relation between LWC and IWC at different stages of cloud development. For the newly developed cell (P4), the high LWC with less IWC (< 0.2 g m^{-3}) was predominant, and this feature was also present at developing stage. The other stages with appreciable IWC corresponded with LWC less than 0.2 g m^{-3}, indicating the clouds with different extents of glaciation. The clouds in P2 were primarily composed of ice water, with the number concentration of cloud droplets significantly lower compared to P1. P3 was identified as dissipating cells, when the clouds were dominated by ice water, and had a higher F_{Ice} than P2 (Fig. 2).

3.2 Ice production at different stages of cloud development

Figure 6 shows the vertical profiles of microphysical properties at different stages. Figure 6a1-a4 and 6c1-c4 are colored by the effective diameter of droplets and $F_{\text{smaller ice}}$, respectively. Several targeting periods of P1, P2, and P4 were selected for detailed analysis, including periods 1.1, 1.2, 2.1, 2.2, 2.3, 4.1, 4.2, 4.3 (specific times are given in Table S1), and the corresponding periods are marked in the time series of Fig. 4. In developing cells, N_{FCDP} tended to decrease with the increase of height, while the diameter of droplets tended to increase (Fig. 6a1), and there was an increase in N_{Round} at two levels (Fig. 6b1). The broadened droplet spectrum at two levels of developing cells was also observed (Fig. S4). The period 1.1 (abbreviated as P1.1, the same for other periods) corresponded to high N_{Ice} with less LWC, and P1.2 corresponded to the region with less ice and some LWC (Fig. 6c1). The size spectrum in Fig. 7a showed the N_{FCDP} and $F_{\mathrm{smaller\ ice}}$ at P1.2 were both higher than P1.1, and precipitation particles had formed at P1.1, whereas P1.2 was still dominated by smaller droplets with few precipitation particles (Fig. 6d1). Clear similarities were observed between the two periods: the N_{round} in both periods was higher than other unmarked periods in P1, and the average N_{Round} exceeded 30 $\mathrm{L^{-1}}$ (Fig. 7a), with the maximum N_{Round} was over 50 $\mathrm{L^{-1}}$ (Fig. 6b1). In addition, the larger size determined by the 2D-S than FCDP was found in Fig. 7, which was due to the lower accuracy for 2D-S to determine the particles in smaller bins (Gurganus and Lawson, 2018; Woods et al., 2018). This may be particularly the case when some small non-spherical ices were present at colder temperatures.

P1.1 and P1.2 showed N_{Ice} up to 256 $\mathrm{L^{-1}}$ and 71 $\mathrm{L^{-1}}$ respectively, by considering the factor of 10, which is the uncertainty pointed out by Demott et al. (2010), the observed ice concentration was still about 2 orders of magnitude higher than the calculated INP in the corresponded temperature regime (Fig. S5). The ice shapes showed to be dominated with plate, irregular and linear ice (Fig. 7a), and the 2D-S images showed the presence of H-shaped ice crystals, and the ice particles exhibited obvious riming characteristic. The ice habits were consistent with the feature of cloud region where SIP is thought to be active (Field et al., 2016), considering the temperature of the environment was within the H–M zone, and the region was rich in supercooled large droplets, the H-M process was most likely active (Crosier et al., 2013; Taylor et al., 2016). The ice production of P1.1 and P1.2 appeared to be triggered by the riming process of large ice particles, and the temperature of two periods also indicated the likely H-M process for SIP during this stage (Fig. 7a). The difference between the two periods was that P1.1 seemed to have completed the SIP process and formed precipitation particles, while there was still a large number of cloud droplets at P1.2 with smaller number of large ice. This might suggest the great number of large ice at P1.1 improved the riming efficiency and increased the riming surface area, leading to more small ice through H-M process and resulting in the consumption of the droplets. However, the dynamic vertical or horizontal transported of ice, e.g. in convective thermals, the ice near cloud-top can be circulated downwards surrounding the convection core, while being transported upward in the convection core (Korolev et al., 2020). This might induce some uncertainty when evaluating the concentration at the aircraft observed position.

Cloud-top height developed to 10.1 km in mature cells, and the temperature at this stage was lower than the H-M temperature regime. P2.1, P2.2 and P2.3 corresponded to areas with high, modest, low concentration of ice in P2, respectively, the N_{Round} decreased gradually from P2.1 to P2.3, and P2.2 had more cloud droplets (Fig. 6a2-d2). The size spectrum in Fig. 7b showed that the N_{Ice}, N_{Round} and $F_{\mathrm{smaller\ ice}}$ at P2.1 were all higher than that at P1.1. The plate, irregular, and linear ice also accounted for the majority of ice at P2.1, and the riming characteristic of large ice at P2.1 was clearly shown in the images (Fig. 7b). Although the average temperature of P2.1 was as low as -11.7 °C, the abundant large ice particles seemed to trigger the active SIP process at P2.1 with high N_{Ice} about 300 L^{-1}, indicating that the SIP process might not be restricted by temperature, though the possible transport of ice from other cloud regions is not able to be completely excluded. The period 2.2 that lacked enough large ice was likely still in the glaciation process, and P2.3 might be difficult to trigger a more active SIP process due to the smaller number of large ice and limited liquid water. It should be noted that the observed N_{Ice} may involve hydrometeors transported from other parts of clouds, along with the locally produced ice. The ice production can therefore be considered as a continuous process and the observed N_{Ice} is a net production of ice after considering all the input (local production and transport in) and output (fall out and transport out) factors at the observation level.

In dissipating cells, the clouds were dominated by ice and $F_{\text{smaller ice}}$ decreased, indicating the ice production process had completed (Fig. 6a3-d3). The clouds in P4 were dominated by liquid water and classified as young cells, with a cloud-top of only 5.5 km (Fig. 6a4-d4). The vertical profiles showed that P4.1 and P4.3 were dominated by droplets with few ice particles and large droplets, while P4.2 was composed of large droplets with few droplets. The ice particles observed at this stage most likely originated from the ice nucleation process and ice falling from above. Aircraft penetrated the cloud-top at P4.3 and observed several ice particles (Fig. 7c), which were likely primary ice particles. The size spectrum and 2D-S images in Fig. 7c showed that large ice particles presented at P4.1, and the images suggested these were likely formed through riming and Bergeron processes, while the ice at P4.2 was mainly smaller ice, possibly still in the process of growth.

The large ice falling from the upper level likely played a very important role in the ice production process, where the primary ice crystals might form through the nucleation process and grow up in the upper level or during the fall, then fall to the lower level to trigger the ice production process. However, the number of large ice particles was not the only factor that determined the ice production process, the large droplet also played a significant role in promoting the SIP process. Figure 8 shows the scatter plots of the corresponding distribution of N_{Ice} and N_{Round} at different stages, colored by the diameter of large droplet. There was a positive correlation between N_{Ice} and N_{Round}, where more large droplets generally corresponded to a higher N_{Ice}. Comparing P1.1 and P1.2, it could be found that the larger large droplet tended to produce a higher N_{Ice} at the same N_{Round}, the large droplet with a diameter of 160 μm corresponded to almost 5-folds ice numbers of that of 80 μm, and Figure 8 also clearly showed the importance of the larger large droplet to produce more ice particles in P2. Based on the above analysis, it could be inferred that when a high number of large ice particles fell from the upper level to the lower level, if there were abundant larger large droplets in the lower level, the riming efficiency could be improved, and then the SIP process could be enhanced.

3.3 Ice production determined by the distance to cloud-top

Figure 4 showed even at the same level, N_{Ice} had two orders of magnitude difference from less than unit to a few hundred per litre. This means during the aircraft penetration, the different intensity of SIP events had been experienced. The primary cause of this variability was attributed to the position of aircraft relative to the cloud-top, i.e. the distance to cloud-top (DCT) for the measurement.

Figure 4b shows the time series of DCT during experiment. When penetrating a cloud turret, the aircraft entered the cloud with a low DCT, reached a higher DCT when close to the convective core, and left the cloud with a low DCT again. It therefore showed a few humps of DCT during a few penetrations of convective cells or more spread part of clouds. The DCT ranged from 0.01 to 4.6 km during experiment. Figure 4b and d showed the higher DCT (2.8 and 4 km, respectively) corresponded to the peak values of N_{Ice} (256 and 300 L^{-1}, respectively) in P1 and P2. For each penetration, N_{Ice} increased dramatically when aircraft was closer to the cloud core with higher DCT, but decreased upon leaving. This clearly indicated the positive correlation between DCT and N_{Ice}.

Figure 9 shows N_{Ice} and N_{FCDP} as functions of DCT for different stages of clouds. At the developing stage, N_{Ice} significantly enhanced when DCT was above 2km, and was positively correlated with N_{Ice} up to DCT of 3km. For the mature and dissipating stage, N_{Ice} was enhanced from the cloud-top (DCT = 0.2 km) to a certain DCT but decreased when larger DCT. This suggested the development of cloud-top increased N_{Ice}, and considering the larger particles tended to fall to cloud base and form precipitation, the reduced N_{Ice} close to cloud base may be due to the coalesce of ice which reduced the number but enlarged the size of ice. It should be noted that the observed clouds have included both widespread stratiform and imbedded convective clouds, and the metric of DCT should all apply. The DCT essentially implies the amount of ice hydrometeors may fall from above, but may not be directly associated with the current updraft strength or turbulence.

N_{Ice} could increase from a few dozens to a few hundreds of numbers per litre, which are all well above the estimation from INP, indicating the strong SIP. For the SIP mechanism, the temperature of P1 (−5 to −8 ºC) was in the typical H-M temperature region, while the temperature of P2 (−12 ºC) was lower than H-M temperature. Even at the same ambient temperature of measurements (because the aircraft penetration was at the same altitude), the N_{Ice} showed a remarkable difference. This suggested that the DCT played an important role in SIP process, and in the region with lower temperature than H-M temperature zone, the DCT tended to be a more important factor than temperature in determining the intensity of SIP. This could be explained by the seeder-feeder mechanism occurring in the stratiform cloud precipitation (Hobbs and Locatelli, 1978; Hobbs et al., 1980; Matejka et al., 1980): when the cloud-top is higher, more primary ice particles form at colder temperatures and fall. The ice particles can capture smaller liquid water droplets when falling, during which they can grow and the fall speed can be accelerated. This process can considerably enhance the interaction between ice and water droplets, or among ice particles, which is necessary for the occurrence of ice fracture hereby leads to the avalanche secondary ice production. The explanation was also similar to the results reported by Li et al. (2021), which showed the columnar ice crystals were produced in the lower level seeded by ice particles falling from the upper level. The age of ice was examined as the fraction of smaller ice ($F_{\mathrm{smaller\ ice}}$) here, with the assumption that a youngly formed ice would have smaller size. This implied the pronounced production of smaller ice by SIP processes with $F_{\mathrm{smaller\ ice}}$ up to 70% during the developing period, while a lower $F_{\mathrm{smaller,ice}}$ (0.2-0.6) indicated the growth of ice and smaller ice was consumed during the dissipating stage. Then the likely schematic plot of ice production at different stages of clouds was given (Fig. 10). The higher cloud-top leads to the formation of more primary ice through the nucleation process, and the ice can grow in the upper level and during the falling. The SIP process is triggered when ice particles in the upper level fall to the lower level with supercooled water, initiating the interactions between ice and droplets. In regions with larger DCT, ice particles in the upper level have sufficient time and distance to grow larger during falling, and the fall speed also can be accelerated, resulting in more and larger ice particles falling to the lower level. Consequently, the intensity of SIP process becomes stronger in this region because the falling large ice particles enhance the interactions between ice and droplets, as well as among ice particles. However, it should be noted that the larger ice particles may also falling to H-M zone in mature cells and trigger the SIP process.

3.4 The production rate of secondary ice

The secondary ice production rate could be estimated through the measured number size distribution of ice (Harris-Hobbs and Cooper, 1987; Crosier et al., 2011). The concentration between the lengths of 90-140 μm ($N_{90\text{-}140\mu\mathrm{m}}$) was divided by the time required for ice to grow under this size range. The ice grew linearly under water supersaturation at this size range and was about 1.4 μm/s under T = −6 ºC (Ryan et al., 1976), resulting in around 35.7 s to grow for 50 μm (τ). It was assumed here that the ice numbers were in a steady state that the smaller ice at size (L) = 90 μm grew to L = 140 μm was replenished by smaller ice newly produced purely by splinters. The production rate of the smaller secondary ice could then be estimated by the ice number between this growth size limit ($N_{90\text{-}140\mathrm{nm}}$) divided by the time required for the growth (τ). Figure S6a showed the measured SIP rate ranged at 0.005-1.8 $\mathrm{L^{-1}\ s^{-1}}$, generally consisted with previous observations at 0.001-1 $\mathrm{L^{-1}\ s^{-1}}$ for cumulus clouds (Harris-Hobbs and Cooper, 1987), 0.043 $\mathrm{L^{-1}\ s^{-1}}$ for stratus cloud embedded with cumulus (Crosier et al., 2011), 0.14 $\mathrm{L^{-1}\ s^{-1}}$ in the mature region of cumulus (Taylor et al., 2016). Based on the observation data of mixed-phase stratiform cloud system over Northern China, Hou et al. (2021) estimated the SIP rate and found the highest concentration of ice splinter could reach 1000 $\mathrm{L^{-1}}$ in five minutes, which implied that the average SIP rate could reach up to 3.3 $\mathrm{L^{-1}\ s^{-1}}$. Figures S6c and S7 showed the rate was positively correlated with the number concentration of large ice (graupel) and large droplet.

The above analysis showed the importance of collision-coalescence process in producing the enhancement of ice number concentration. The collision-coalescence model had previously been used to calculate the production rate of secondary ice. It was essentially determined by the collision-coalescence between graupel and droplet above certain size. It was long established in the laboratory that only droplet > 25 μm in diameter could produce secondary ice when rimmed on the graupel. The SIP rate could therefore be calculated from the collision-coalescence process between graupel and droplet (Reisner et al., 1998), and the model calculated equation is described as:

$$P = \pi/4 \cdot (D_{\mathrm{graupel}} + D_{\mathrm{droplet}})^2 N(D_{\mathrm{graupel}}) N(D_{\mathrm{droplet}}) E |U_{\mathrm{graupel}} - U_{\mathrm{droplet}}| , \tag{3}$$

where D_{graupel} and D_{droplet} are the effective diameter (which is the third divided by the second moment of size distribution) of graupel and droplet respectively, and $N(D_{\mathrm{graupel}})$ and $N(D_{\mathrm{droplet}})$ are the number concentration of graupel and droplet respectively; U_{graupel} and U_{droplet} represent the terminal velocities, which are calculated as the absolute difference between graupel and droplet, as $U_{\mathrm{graupel}} = 7\times10^2 D_{\mathrm{graupel}}$, $U_{\mathrm{droplet}} = 3\times10^7 D_{\mathrm{droplet}}$. E is the collection efficiency among the size bins of graupel and droplet, which was assumed to be 1 for the first instance but would be discussed as follows. The ice particle with *d* > 250 μm was considered as graupel which was able to efficiently capture droplet (Harris-Hobbs and Cooper, 1987). Here the effective radius (Re) was used to represent the size distribution of graupel/droplet within a time window to simplify the calculation of collision among size bins. The Re was used rather than median mass value from the size distribution was because the former was determined by the cross section of particles (and the collection by collision-coalescence process was also determined by area), and weighted towards larger particles. Ice particles were observed to be mostly rimed in images, hereby all ice particles with *d* > 250 μm were considered to be graupels that already accreted by small droplets (i.e. *d* < 13 μm), but not calculated the fraction of rimmed surface (Harris-Hobbs and Cooper, 1987). Considering that the observation here was actually after the SIP process was initialized, when the smaller cloud droplets had been considerably consumed and most ice particles were rimed, the number of large droplets (*d* > 50 μm) was the limited factor for SIP, and therefore used to calculate the modelled SIP rate.

Figure S6a shows the time series of modelled SIP rate, which was well correlated with measured SIP (correlation coefficient was 0.86), the ratio between Re of large droplets and graupels ($\mathrm{Re}_{\mathrm{Round}}$ / $\mathrm{Re}_{\mathrm{Graupel}}$) ranged from 0.1-0.8 (Fig. S6b). Figure 11 investigated the correlation between measured and modelled SIP rate, colored by $\mathrm{Re}_{\mathrm{Round}}$ / $\mathrm{Re}_{\mathrm{Graupel}}$. According to Eq. (3), the collection efficiency $E = 1$ was firstly considered which gave the upper limit for the calculation, but any other circumstances would cause $E < 1$ and reduced the model results. The model was closed to the observation when $\mathrm{Re}_{\mathrm{Round}}$ / $\mathrm{Re}_{\mathrm{Graupel}}$ ranged at 0.4-1 (slope=0.94), but model started to overestimate compared to observation when $\mathrm{Re}_{\mathrm{Round}}$ / $\mathrm{Re}_{\mathrm{Graupel}}$ decreased (shown by the datapoints grouped as different levels of $\mathrm{Re}_{\mathrm{Round}}$ / $\mathrm{Re}_{\mathrm{Graupel}}$). This clearly indicated reduced *E* when reduced $\mathrm{Re}_{\mathrm{Round}}$ / $\mathrm{Re}_{\mathrm{Graupel}}$. *E* was then further adjusted to give the modelled SIP rate matched with observation at different levels of $\mathrm{Re}_{\mathrm{Round}}$ / $\mathrm{Re}_{\mathrm{Graupel}}$, shown in the sub-plot of Fig. 11. A linearly increased collection efficiency was found, when *E* increased from 0.2 to 1 with $\mathrm{Re}_{\mathrm{Round}}$ / $\mathrm{Re}_{\mathrm{Graupel}}$ increased from 0.1 to 0.7. This was consisted with the theory of droplet collision, when the collector particle approaches the droplet, the droplet tends to follow the streamline around the collector particle and may avoid collision (Wallace and Hobbs, 2006; Pruppacher and Klett, 2010). The collision efficiency was small when the collector particle was much larger than the droplet, because too small particles would follow the streamline around collector particle due to small inertia, and the collision efficiency increased with increased droplet size because droplets with greater inertia tended to follow a straight line. The results here implied that the SIP rate could be well explained by the collision theory between graupel and large droplet, and the availability of both numbers and the chance for their collision were the factors in determining the SIP rate.

4 Conclusion

In this study, we investigated the ice production of stratiform clouds with embedded convection during an extratropical cyclone over the North China Plain, through in-situ measurements of the microphysical properties. The aircraft penetrated four stages during the lifecycle of the clouds including the developing, mature, dissipating and young cells. The four relative stages were identified by ice mass fraction, by considering a more mature cloud has a more glaciated fraction. In developing cells, high N_{Ice} and LWC-rich region were observed, the ice mass fraction in clouds spanned from zero (pure water) to unit (pure ice). In mature cells, a higher glaciation extent was observed, with ice mass fraction ranging from 0.36 to 1, and N_{Ice} reaching up to 300 L^{-1} at this stage. The dissipating cells were dominated by ice but only intermittent unglaciated LWC-rich clouds, and the ice mass fraction ranged in 0.56-1. The young stage was rich of LWC with lower ice mass fraction. The number concentration of ice was found to frequently well exceeds that from ice nucleation, reaching up to a few hundred per litre, indicating the strong secondary ice production (SIP).

The possible seeder-feeder process was found to extend the SIP process beyond the slightly supercooled temperature region for the typically considered H-M process. The intensity of SIP was to the first order determined by the numbers of graupel and droplets, because the collision and coalescence among these hydrometeors necessitated the fracture of ice. The modelled and measurement-based calculations showed appropriately treating the size distribution hereby the determination of collection efficiency will improve the modelling of the SIP rate. Importantly, the results showed the generally enhanced SIP when larger distance to cloud-top, which means once the cloud-top reached sufficient height, the initialized ice from nucleation may boost the avalanche glaciation process when falling ice reached lower levels in cloud. It should be noted that whether the falling hydrometeors were the ones generated by the ice production process or were about to participate in the ice production process at the same level, may never be separated due to the short time-scale of the collision process. However, this is a continuous process which may involve both the already-formed and ongoing-happening particles, and the observed or modelled results are an overall net production of ice. The ice particles falling from aloft increase the numbers of graupels and collision chance between graupel and droplets, and then trigger the SIP process, therefore the seeder-feeder and SIP process may occur simultaneously after SIP process has initialized. The results about the microphysical properties of stratiform clouds with convective cells under different stages suggest the falling hydrometeors associated with cloud-top height importantly controlled the cloud glaciation and precipitation process, and this may also help find the region of supercooled water of clouds for the weather modification work.

Data availability

The data in this study are available from the authors upon request.

Author contribution

YD and DL analyzed the data and wrote the manuscript, and this work was completed under the guidance of DL, MH and DD. DeZ, PT, WX, WZ, HH, BP, YJ, JS and FW contributed to the aircraft data processing and analysis. DW, XL and YC performed the synoptic analysis. DoZ and YH contributed to the radar data processing and analysis. RZ conducted the shape classification of 2D-S images.

Competing interests

At least one of the (co-)authors is a member of the editorial board of *Atmospheric Chemistry* and *Physics*. The authors also have no other competing interests to declare.

Acknowledgements

This research was supported by the National Natural Science Foundation of China (Grant Nos. 42205093, 42075084, 42005078).

References

Bacer, S., Sullivan, S. C., Sourdeval, O., Tost, H., Lelieveld, J., and Pozzer, A.: Cold cloud microphysical process rates in a global chemistry–climate model, Atmospheric Chemistry and Physics, 21, 1485-1505, 10.5194/acp-21-1485-2021, 2021.

Beswick, K. M., Gallagher, M. W., Webb, A. R., Norton, E. G., and Perry, F.: Application of the Aventech AIMMS20AQ airborne probe for turbulence measurements during the Convective Storm Initiation Project, Atmospheric Chemistry and Physics, 8, 5449-5463, 2008.

Cai, Y., Snider, J. R., and Wechsler, P.: Calibration of the passive cavity aerosol spectrometer probe for airborne determination of the size distribution, Atmospheric Measurement Techniques, 6, 2349-2358, 10.5194/amt-6-2349-2013, 2013.

Cantrell, W. and Heymsfield, A.: Production of Ice in Tropospheric Clouds: A Review, Bulletin of the American Meteorological Society, 86, 795-808, 10.1175/bams-86-6-795, 2005.

Coopman, Q., Hoose, C., and Stengel, M.: Analysis of the Thermodynamic Phase Transition of Tracked Convective Clouds Based on Geostationary Satellite Observations, Journal of Geophysical Research: Atmospheres, 125, 10.1029/2019jd032146, 2020.

Crosier, J., Choularton, T. W., Westbrook, C. D., Blyth, A. M., Bower, K. N., Connolly, P. J., Dearden, C., Gallagher, M. W., Cui, Z., and Nicol, J. C.: Microphysical properties of cold frontal rainbands†, Quarterly Journal of the Royal Meteorological Society, 140, 1257-1268, 10.1002/qj.2206, 2013.

Crosier, J., Bower, K. N., Choularton, T. W., Westbrook, C. D., Connolly, P. J., Cui, Z. Q., Crawford, I. P., Capes, G. L., Coe, H., Dorsey, J. R., Williams, P. I., Illingworth, A. J., Gallagher, M. W., and Blyth, A. M.: Observations of ice multiplication in a weakly convective cell embedded in supercooled mid-level stratus, Atmospheric Chemistry and Physics, 11, 257-273, 10.5194/acp-11-257-2011, 2011.

DeMott, P. J., Prenni, A. J., Liu, X., Kreidenweis, S. M., Petters, M. D., Twohy, C. H., Richardson, M. S., Eidhammer, T., and Rogers, D. C.: Predicting global atmospheric ice nuclei distributions and their impacts on climate, Proc Natl Acad Sci U S A, 107, 11217-11222, 10.1073/pnas.0910818107, 2010.

Field, P. R., Lawson, R. P., Brown, P. R. A., Lloyd, G., Westbrook, C., Moisseev, D., Miltenberger, A., Nenes, A., Blyth, A., Choularton, T., Connolly, P., Buehl, J., Crosier, J., Cui, Z., Dearden, C., DeMott, P., Flossmann, A., Heymsfield, A., Huang, Y., Kalesse, H., Kanji, Z. A., Korolev, A., Kirchgaessner, A., Lasher-Trapp, S., Leisner, T., McFarquhar, G., Phillips, V., Stith, J., and Sullivan, S.: Secondary Ice Production - current state of the science and recommendations for the future, Meteorological Monographs, 10.1175/amsmonographs-d-16-0014.1, 2016.

Gurganus, C. and Lawson, P.: Laboratory and Flight Tests of 2D Imaging Probes: Toward a Better Understanding of Instrument Performance and the Impact on Archived Data, Journal of Atmospheric and Oceanic Technology, 35, 1533-1553, 10.1175/jtech-d-17-0202.1, 2018.

Hallett, J. and Mossop, S. C.: Production of Secondary ice particles during the riming process, Nature, 249, 26–28, doi:10.1038/249026a0., 1974.

Harris-Hobbs, R. L. and Cooper, W. A.: Field evidence supporting quantitative predictions of secondary ice production rates, journal of the atmospheric sciences, 44, 1071-1082, 1987.

Hobbs, P. V. and Locatelli, J. D.: Rainbands, Precipitation Cores and Generating Cells in a Cyclonic Storm, Journal of Atmospheric Sciences, 35, 230-241, 1978.

Hobbs, P. V., Matejka, T. J., Herzegh, P. H., Locatelli, J. D., and Houze , R. A.: The Mesoscale and Microscale Structure and Organization of Clouds and Precipitation in Midlatitude Cyclones. I: A Case Study of a Cold Front, Journal of Atmospheric Sciences, 37, 568-596, 1980.

Hogan, R. J., Field, P. R., Illingworth, A. J., Cotton, R. J., and Choularton, T. W.: Properties of embedded convection in warm-frontal mixed-phase cloud from aircraft and polarimetric radar, Quarterly Journal of the Royal Meteorological Society: A journal of the atmospheric sciences, applied meteorology and physical oceanography, 128, 451-476, 2002.

Holroyd, E. W.: Some Techniques and Uses of 2D-C Habit Classification Software for Snow Particles, Journal of Atmospheric and Oceanic Technology, 4, 498–511, 1987.

Hou, T., Lei, H., He, Y., Yang, J., Zhao, Z., and Hu, Z.: Aircraft Measurements of the Microphysical Properties of Stratiform Clouds with Embedded Convection, Advances in Atmospheric Sciences, 38, 966-982, 10.1007/s00376-021-0287-8, 2021.

Hou, T., Chen, B., Zhou, X., Zhao, C., Feng, Q., Yan, F., Zhou, W., Cui, Y., Du, Y., Li, Z., Zhao, D., and Ma, X.: Aircraft-based observations of ice concentrations in a midlatitude mixed-phase stratiform cloud system with embedded convection, Atmospheric Research, 281, 10.1016/j.atmosres.2022.106471, 2023.

Huang, Y., Blyth, A. M., Brown, P. R. A., Choularton, T. W., Connolly, P., Gadian, A. M., Jones, H., Latham, J., Cui, Z., and Carslaw, K.: The development of ice in a cumulus cloud over southwest England, New Journal of Physics, 10, 10.1088/1367-2630/10/10/105021, 2008.

Jiang, Y. and Liu, L.: A test pattern identification algorithm and its application to CINRAD/SA(B) data, Advances in Atmospheric Sciences, 31, 331-343, 10.1007/s00376-013-2315-9, 2014.

Kanji, Z. A., Ladino, L. A., Wex, H., Boose, Y., Burkert-Kohn, M., Cziczo, D. J., and Krämer, M.: Overview of Ice Nucleating Particles, Meteorological Monographs, 58, 1.1-1.33, 10.1175/amsmonographs-d-16-0006.1, 2017.

Korolev, A. and Isaac, G. A.: Relative humidity in liquid, mixed-phase, and ice clouds., Journal of the atmospheric sciences, 63, 2865-2880, 2006.

Korolev, A., DeMott, P. J., Heckman, I., Wolde, M., Williams, E., Smalley, D. J., and Donovan, M. F.: Observation of secondary ice production in clouds at low temperatures, Atmospheric Chemistry and Physics, 22, 13103-13113, 10.5194/acp-22-13103-2022, 2022.

Korolev, A., Heckman, I., Wolde, M., Ackerman, A. S., Fridlind, A. M., Ladino, L. A., Lawson, R. P., Milbrandt, J., and Williams, E.: A new look at the environmental conditions favorable to secondary ice production, Atmospheric Chemistry and Physics, 20, 1391-1429, 10.5194/acp-20-1391-2020, 2020.

Korolev, A., McFarquhar, G., Field, P. R., Franklin, C., Lawson, P., Wang, Z., Williams, E., Abel, S. J., Axisa, D., Borrmann, S., Crosier, J., Fugal, J., Krämer, M., Lohmann, U., Schlenczek, O., Schnaiter, M., and Wendisch, M.: Mixed-Phase Clouds: Progress and Challenges, Meteorological Monographs, 58, 5.1-5.50, 10.1175/amsmonographs-d-17-0001.1, 2017.

Lance, S., Brock, C. A., Rogers, D., and Gordon, J. A.: Water droplet calibration of the Cloud Droplet Probe (CDP) and in-flight performance in liquid, ice and mixed-phase clouds during ARCPAC, Atmospheric Measurement Techniques, 3, 1683-1706, 10.5194/amt-3-1683-2010, 2010.

Lau, K. M. and Wu, H. T.: Warm rain processes over tropical oceans and climate implications, Geophysical Research Letters, 30, 10.1029/2003gl018567, 2003.

Lawson, R. P. and Cooper, W. A.: Performance of some airborne thermometers in clouds, Journal of Atmospheric and Oceanic Technology, 7, 480–494, 10.1175/1520-0426(1990)007,0480:POSATI.2.0.CO;2, 1990.

Lawson, R. P. and Rodi, A. R.: A New Airborne Thermometer for Atmospheric and Cloud Physics Research. Part I: Design and Preliminary Flight Tests, Journal of Atmospheric and Oceanic Technology, 9, 556-574, 1992.

Lawson, R. P., Stewart, R. E., and Angus, L. J.: Observations and Numerical Simulations of the Origin and Development of Very Large Snowflakes, Journal of the Atmospheric Sciences, 55, 1998.

Lawson, R. P., Woods, S., and Morrison, H.: The Microphysics of Ice and Precipitation Development in Tropical Cumulus Clouds, Journal of the Atmospheric Sciences, 72, 2429-2445, 10.1175/jas-d-14-0274.1, 2015.

Lawson, R. P., O'Connor, D., Zmarzly, P., Weaver, K., Baker, B., Mo, Q., and Jonsson, H.: The 2D-S (Stereo) Probe: Design and Preliminary Tests of a New Airborne, High-Speed, High-Resolution Particle Imaging Probe, Atmospheric and Oceanic Technology, 23, 1462–1477, 2006.

Lenschow, D. H. and Pennell, W. T.: On the measurement of in-cloud and wet-bulb temperatures from an aircraft, Monthly Weather Review, 102, 447-454, 1974.

Lensky, I. and Rosenfeld, D.: The time-space exchangeability of satellite retrieved relations between cloud top temperature and particle effective radius, Atmospheric Chemistry and Physics, 6, 2887-2894, 2006.

Li, H., Möhler, O., Petäjä, T., and Moisseev, D.: Two-year statistics of columnar-ice production in stratiform clouds over Hyytiälä, Finland: environmental conditions and the relevance to secondary ice production, Atmospheric Chemistry and Physics, 21, 14671-14686, 10.5194/acp-21-14671-2021, 2021.

Li, Z., Lau, W. K. M., Ramanathan, V., Wu, G., Ding, Y., Manoj, M. G., Liu, J., Qian, Y., Li, J., Zhou, T., Fan, J., Rosenfeld, D., Ming, Y., Wang, Y., Huang, J., Wang, B., Xu, X., Lee, S. S., Cribb, M., Zhang, F., Yang, X., Zhao, C., Takemura, T., Wang, K., Xia, X., Yin, Y., Zhang, H., Guo, J., Zhai, P. M., Sugimoto, N., Babu, S. S., and Brasseur, G. P.: Aerosol and monsoon climate interactions over Asia, Reviews of Geophysics, 54, 866-929, 10.1002/2015rg000500, 2016.

Liu, Q., Liu, D., Gao, Q., Tian, P., Wang, F., Zhao, D., Bi, K., Wu, Y., Ding, S., Hu, K., Zhang, J., Ding, D., and Zhao, C.: Vertical characteristics of aerosol hygroscopicity and impacts on optical properties over the North China Plain during winter, Atmospheric Chemistry and Physics, 20, 3931-3944, 10.5194/acp-20-3931-2020, 2020.

Lloyd, G., Dearden, C., Choularton, T. W., Crosier, J., and Bower, K. N.: Observations of the Origin and Distribution of Ice in Cold, Warm, and Occluded Frontal Systems during the DIAMET Campaign, Monthly Weather Review, 142, 4230-4255, 10.1175/mwr-d-13-00396.1, 2014.

Locatelli, J. D., Stoelinga, M. T., and Woods, C. P.: Size Spectra of Snow Particles Measured in Wintertime Precipitation in the Pacific Northwest, Journal of the Atmospheric Sciences, 65, 189-205, 10.1175/2007jas2243.1, 2008.

Lohmann, U. and Feichter, J.: Global indirect aerosol effects: a review, Atmos. Chem. Phys., 5, 715–737, https://doi.org/10.5194/acp-5-715-2005, 2005.

Lu, C., Liu, Y., Niu, S., and Vogelmann, A. M.: Observed impacts of vertical velocity on cloud microphysics and implications for aerosol indirect effects, Geophysical Research Letters, 39, 10.1029/2012gl053599, 2012.

Matejka, T. J., Houze, R. A., and Hobbs, P. V.: Microphysics and dynamics of clouds associated with mesoscale rainbands in extratropical cyclones, Quarterly Journal of the Royal Meteorological Society, 106, 29–56, 10.1002/qj.49710644704 1980.

McFarquhar, G. M., Baumgardner, D., and Heymsfield, A. J.: Background and Overview, Meteorological Monographs, 58, v-ix, 10.1175/amsmonographs-d-16-0018.1, 2017.

Mossop, S. C.: Secondary ice particle production during rime growth: The effect of drop size distribution and rimer velocity, Quarterly Journal of the Royal Meteorological Society, 111, 1113-1124, 1985.

Mülmenstädt, J., Sourdeval, O., Delanoë, J., and Quaas, J.: Frequency of occurrence of rain from liquid-, mixed-, and ice-phase clouds derived from A-Train satellite retrievals, Geophysical Research Letters, 42, 6502-6509, 10.1002/2015gl064604, 2015.

Pruppacher, H. R. and Klett, J. D.: Microphysics of Clouds and Precipitation, Springer2010.

Rangno, A. L. and Hobbs, P. V.: Ice particles in stratiform clouds in the Arctic and possible mechanisms for the production of high ice concentrations, Journal of Geophysical Research: Atmospheres, 106, 15065-15075, 10.1029/2000jd900286, 2001.

Reisner, J., Rasmussen, R. M., and Bruintjes, R. T.: Explicit forecasting of supercooled liquid water in winter storms using the MM5 mesoscale model, Quarterly Journal of the Royal Meteorological Society, 124, 1071–1107, https://doi.org/10.1002/qj.49712454804, 1998.

Ryan, B. F., Wishart, E. R., and Shaw, D. E.: Growth Rates and Densities of Ice Crystals between −3°C and −21°C, Journal of Atmospheric Sciences, 33, 842-850, 1976.

Taylor, J. W., Choularton, T. W., Blyth, A. M., Liu, Z., Bower, K. N., Crosier, J., Gallagher, M. W., Williams, P. I., Dorsey, J. R., Flynn, M. J., Bennett, L. J., Huang, Y., French, J., Korolev, A., and Brown, P. R. A.: Observations of cloud microphysics and ice formation during COPE, Atmospheric Chemistry and Physics, 16, 799-826, 10.5194/acp-16-799-2016, 2016.

Tian, P., Liu, D., Zhao, D., Yu, C., Liu, Q., Huang, M., Deng, Z., Ran, L., Wu, Y., Ding, S., Hu, K., Zhao, G., Zhao, C., and Ding, D.: In situ vertical characteristics of optical properties and heating rates of aerosol over Beijing, Atmospheric Chemistry and Physics, 20, 2603-2622, 10.5194/acp-20-2603-2020, 2020.

Wallace, J. M. and Hobbs, P. V.: Atmospheric Science: An Introductory Survey, Elsevier2006.

Wang, D., Duan, Y., Liu, Y., Liang, Z., Liu, C., Zhao, Y., Zhang, Y., Yin, J., and Wang, H.: A case study of the November 2012 mixed rain-snow storm over North China, Acta Meteorologica Sinica, 27, 601-625, 10.1007/s13351-013-0512-1, 2014.

Woods, S., Lawson, R. P., Jensen, E., Bui, T. P., Thornberry, T., Rollins, A., Pfister, L., and Avery, M.: Microphysical Properties of Tropical Tropopause Layer Cirrus, Journal of Geophysical Research: Atmospheres, 123, 6053-6069, 10.1029/2017jd028068, 2018.

Yang, J., Lei, H., and Hou, T.: Observational evidence of high ice concentration in a shallow convective cloud embedded in stratiform cloud over North China, Advances in Atmospheric Sciences, 34, 509-520, 10.1007/s00376-016-6079-x, 2017.

Yuan, T., Martins, J. V., Li, Z., and Remer, L. A.: Estimating glaciation temperature of deep convective clouds with remote sensing data, Geophysical Research Letters, 37, 10.1029/2010gl042753, 2010.

Zhang, R., Li, H., Zhou, X., Li, H., Hu, X., and Xia, Q.: Shape Recognition of DMT Airborne Cloud Particle Images and Its Application, JOURNAL OF APPLIED METEOROLOGICAL SCIENCE 32, 735-747, 10.11898/1001-7313.20210608, 2021.

Zhao, C., Chen, Y., Li, J., Letu, H., Su, Y., Chen, T., and Wu, X.: Fifteen-year statistical analysis of cloud characteristics over China using Terra and Aqua Moderate Resolution Imaging Spectroradiometer observations, International Journal of Climatology, 39, 2612-2629, 10.1002/joc.5975, 2019.

Zuo, D., Liu, D., Zhao, D., Yang, L., Chen, Y., Zhou, W., Huang, M., He, H., Tian, P., Du, Y., Xiao, W., Li, R., Li, J., Gao, Y., Lu, J., Tang, Q., Wang, W., and Ding, D.: Liquid water determination by airborne millimeter cloud radar and in-situ size distribution measurements, Atmospheric Research, 284, 10.1016/j.atmosres.2023.106607, 2023.

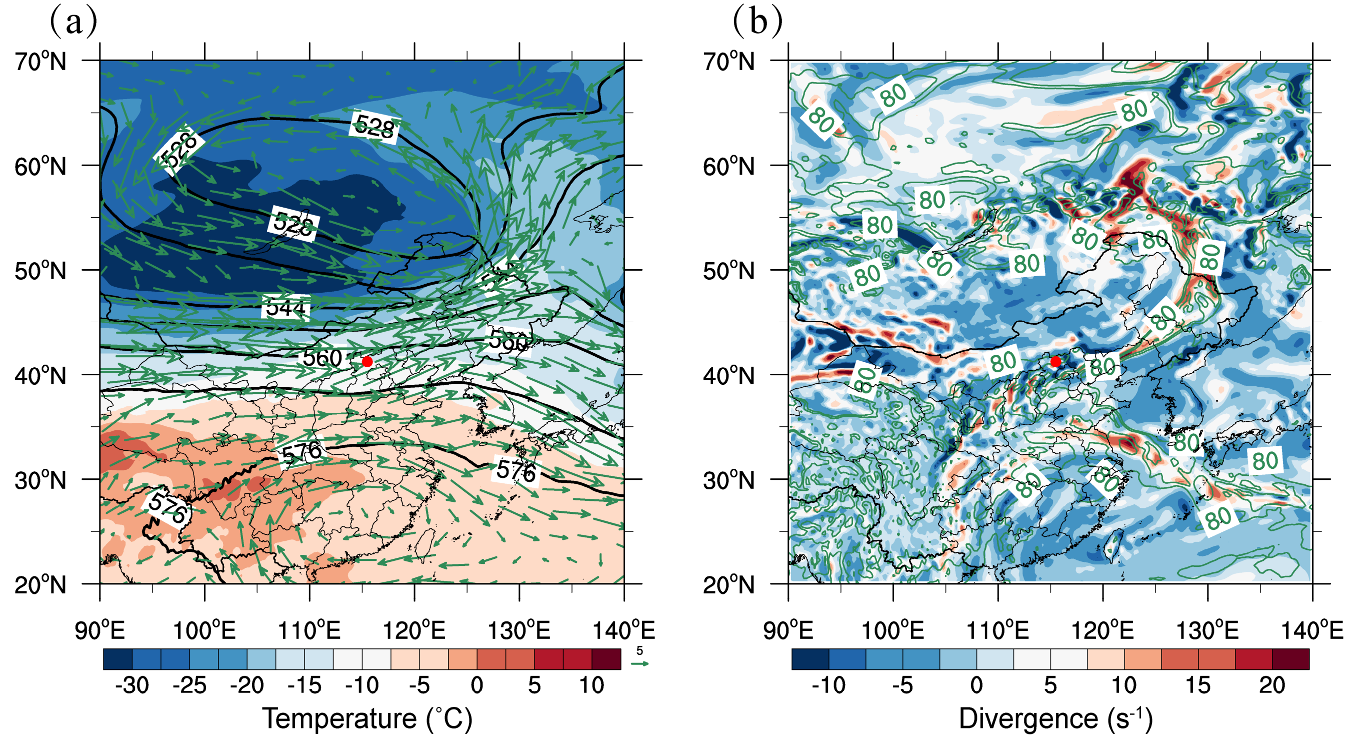

Figure 1: Synoptic overview during experiment. (a) The 500hPa temperature (color), height field (contour), wind field (arrow) at 08:00 (UTC+8h) on September 26th, 2017; (b) 850hPa divergence field (color), relative humidity (green line, only >80% is shown). The experimental region is indicated by the red dot on each plot.

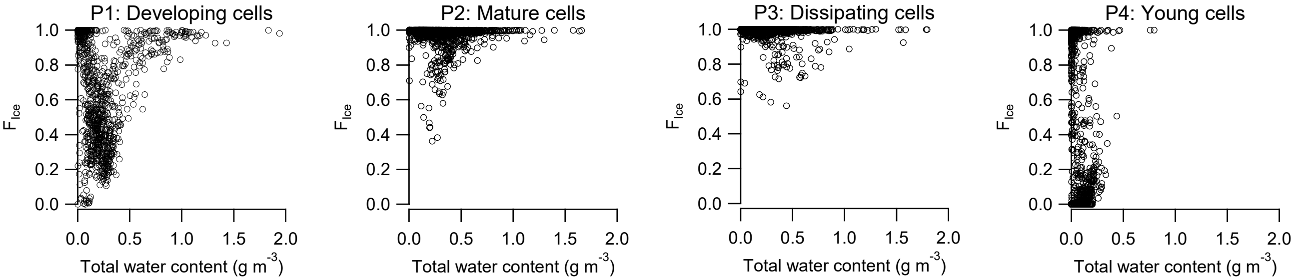

Figure 2: Ice mass fraction (F_{Ice}) as a fuction of total water content at four stages.

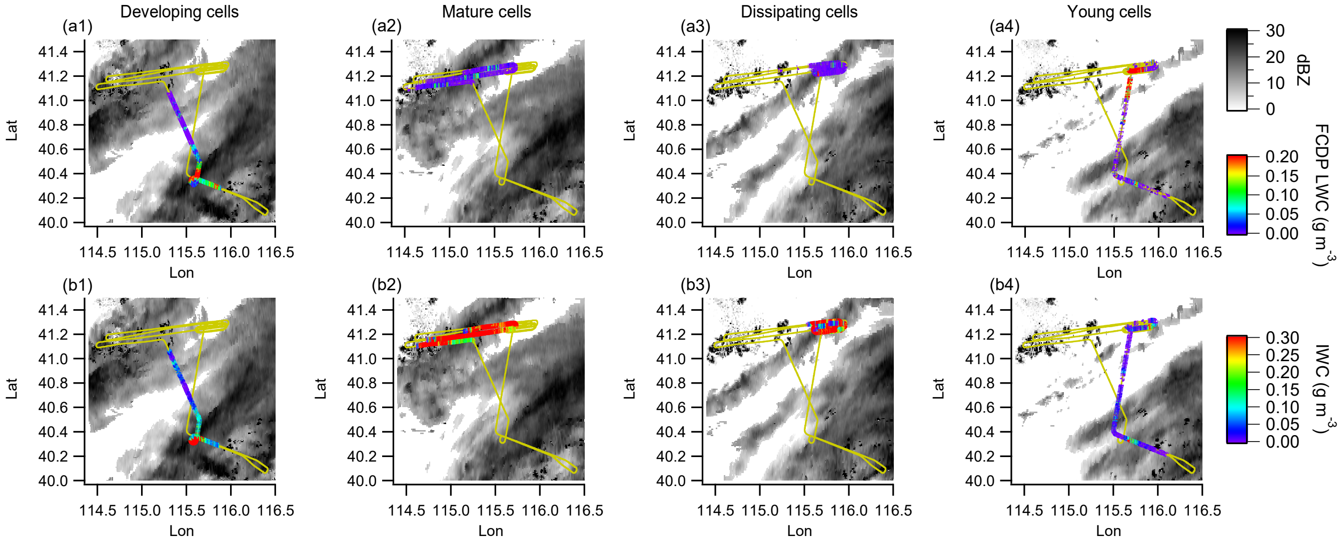

Figure 3: Flight tracks mapping on the composite reflectivity of S-band precipitation radar at different stages of clouds (from left to right). (a) colored by liquid water content (LWC) from the FCDP, (b) colored by ice water content (IWC) from the 2D-S.

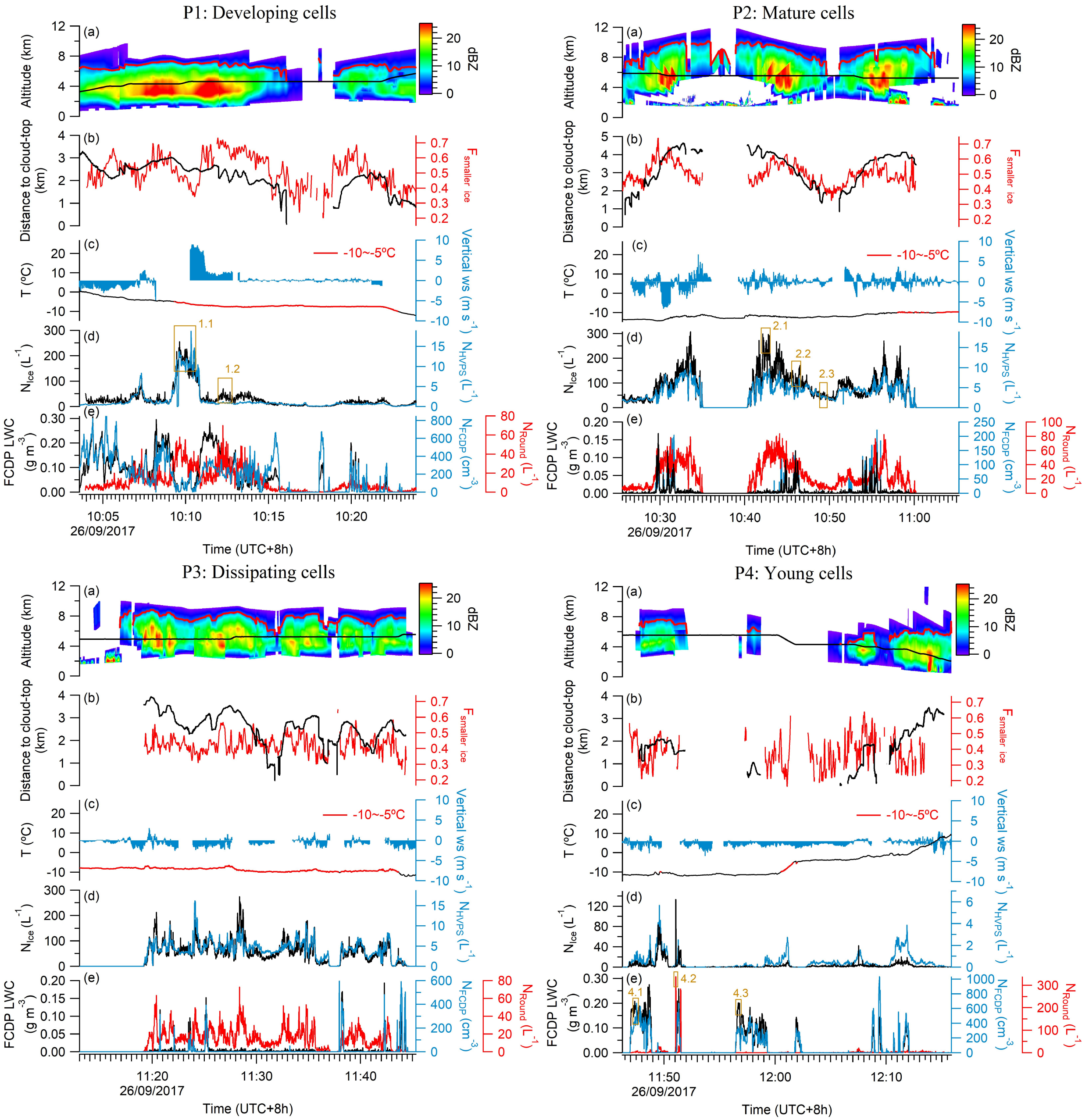

Figure 4: Cloud properties along the flight track at four stages. (a) Vertical profile of radar reflectivity from the ground S-band precipitation radar collocating with the flight path. (b)The distance to cloud-top of aircraft and smaller ice (d < 180 μm) number fraction ($F_{\mathrm{smaller\ ice}}$). (c) Ambient temperature and vertical wind speed. (d) Ice number concentration (N_{Ice}) from the 2D-S and precipitation particle number concentration (N_{HVPS}) from the HVPS. (e) LWC and cloud droplet number concentration (N_{FCDP}) from the FCDP, and the large droplet number concentration (N_{Round}) from the 2D-S. The targeting periods are indexed for further analysis.

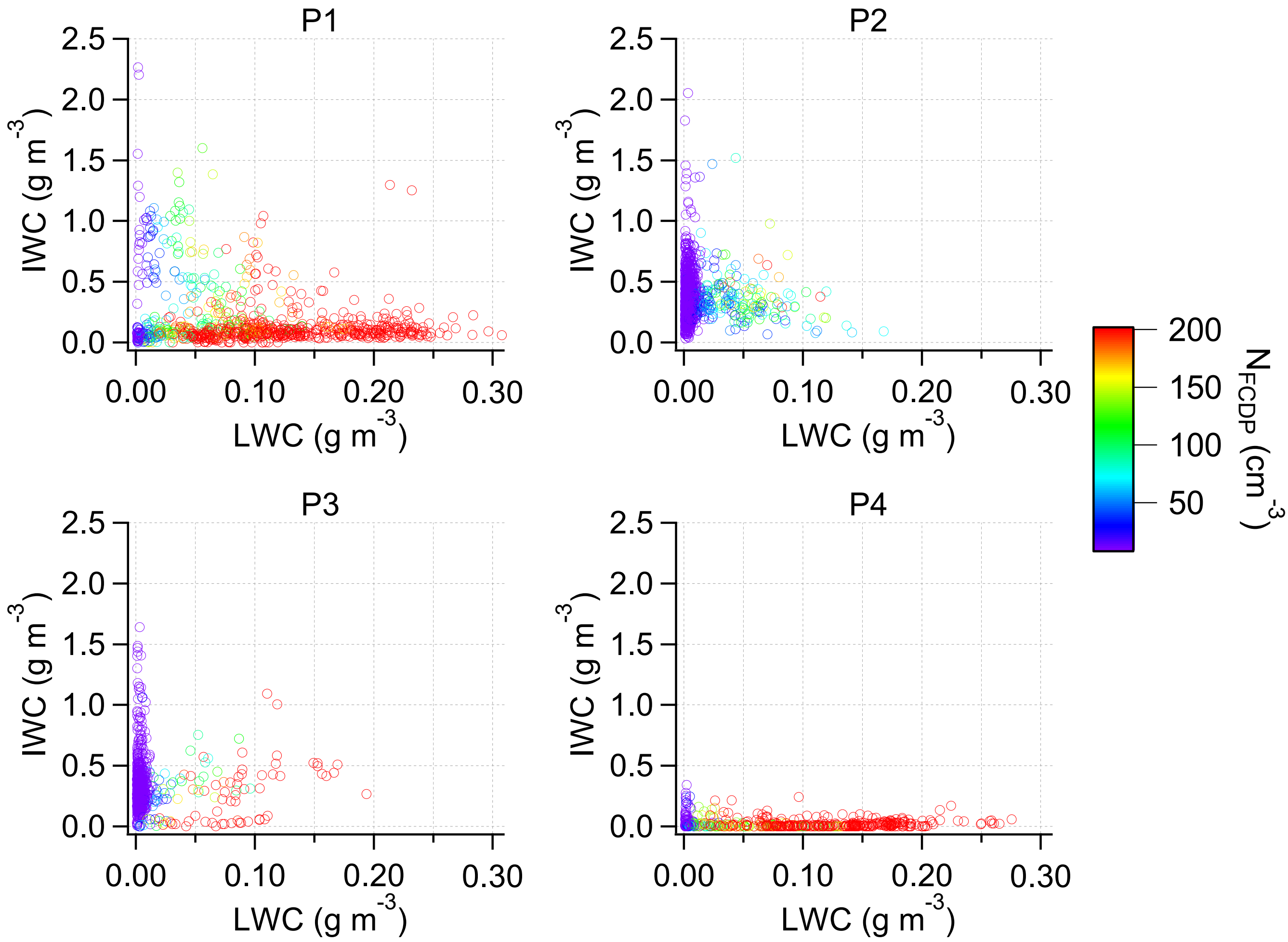

Figure 5: LWC as a function of IWC at different stages of clouds, colored by N_{FCDP}.

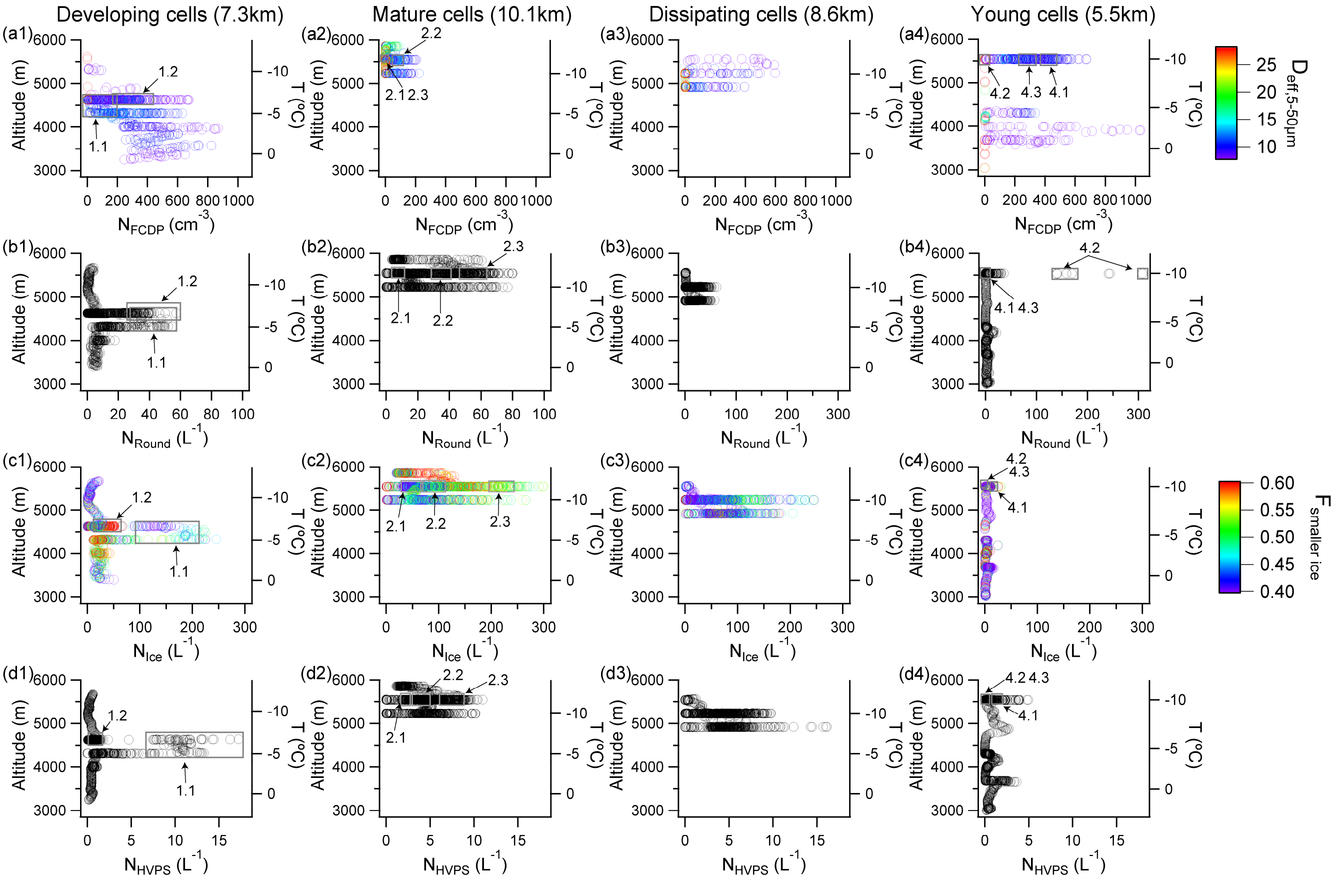

Figure 6: Vertical distributions of hydrometeors at different stages of clouds. (a) N_{FCDP} colored by the effective diameter of droplet (5-50 µm), (b) N_{Round}, (c) N_{Ice} colored by $F_{smaller\ ice}$, (d) N_{HVPS}. The corresponding indexed events in timeseries are marked in this figure, and the cloud-top height was indicated in title brackets.

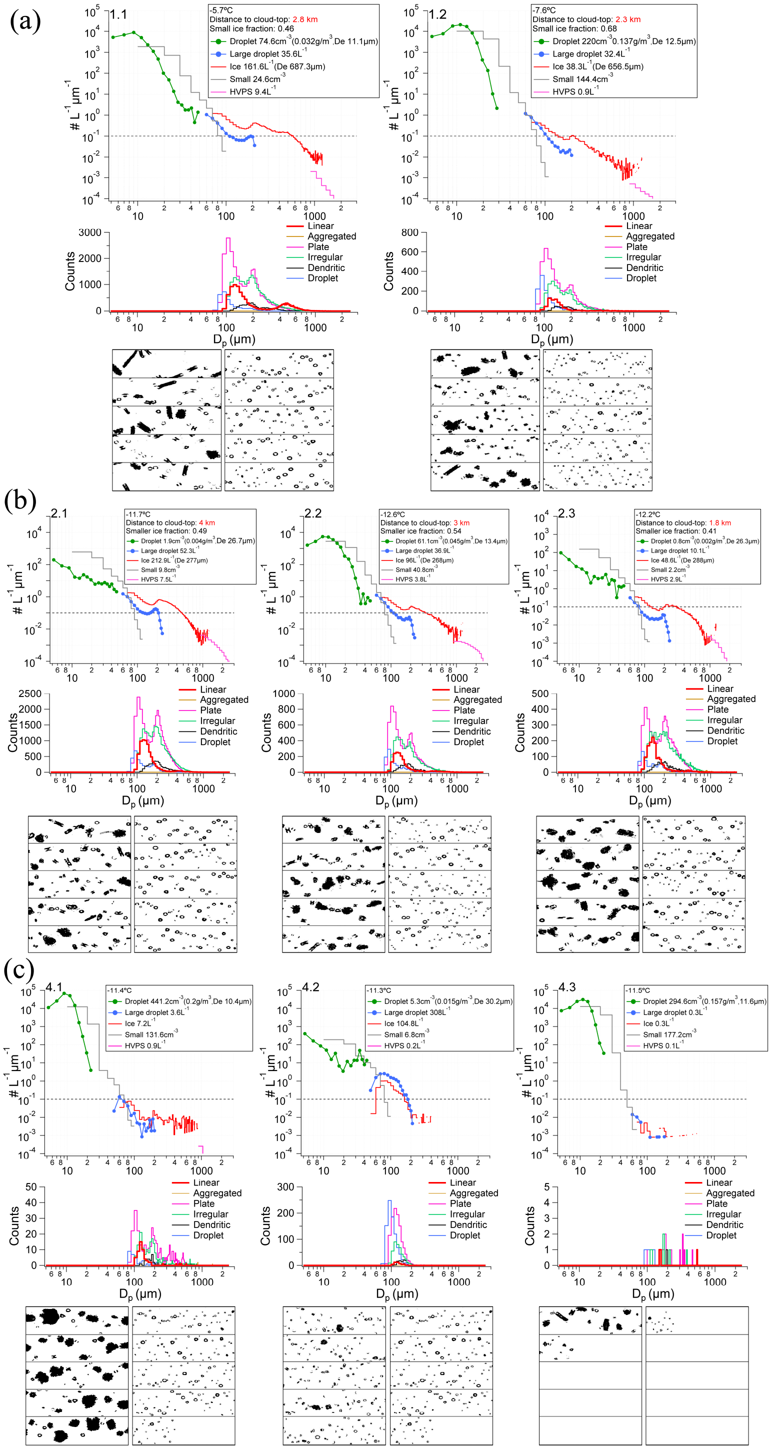

Figure 7: Particle size spectrum from airborne particle spectrum probes, the 2D-S images and the shape classification results of 2D-S images (a) periods 1.1 and 1.2, (b) periods 2.1, 2.2 and 2.3, (c) periods 4.1, 4.2 and 4.3.

680

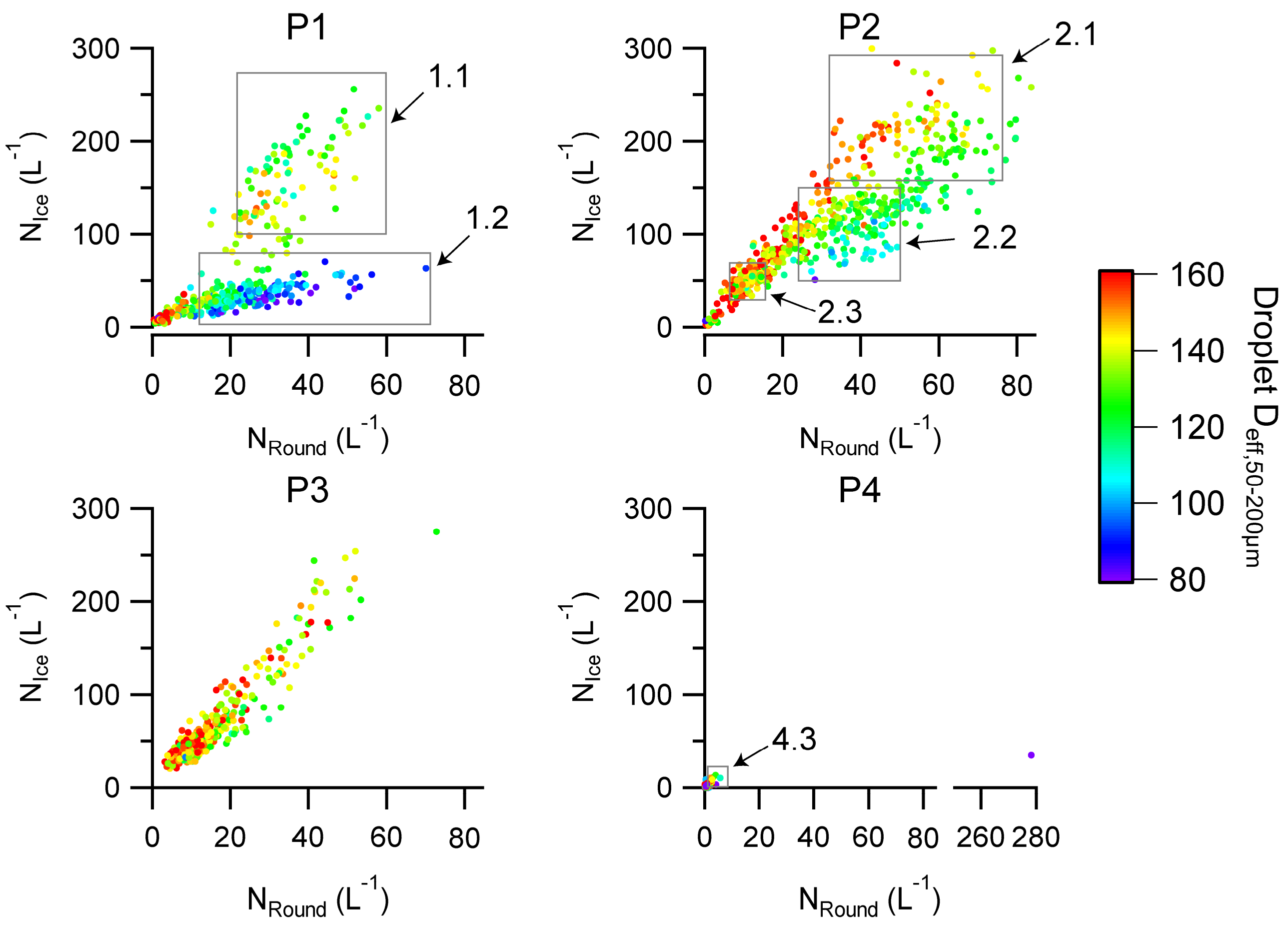

Figure 8: ***N*$_{\text{Round}}$ as a function of *N*$_{\text{Ice}}$ at different stages, colored by the diameter of large droplet (50-200 µm).**

685

690

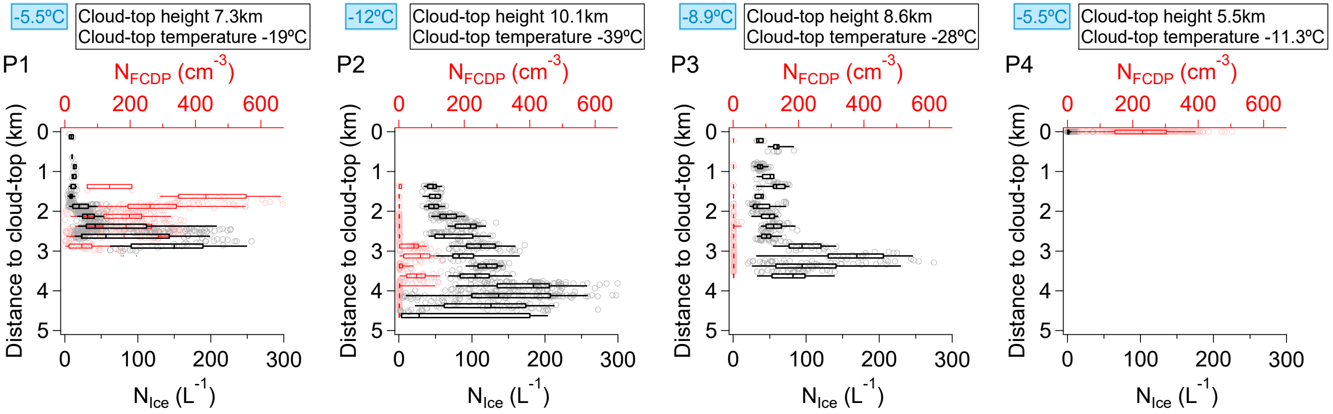

Figure 9: N_{FCDP} and N_{Ice} as functions of distance to cloud-top. Gray circled markers and black boxes represent N_{Ice}, light red circled markers and red boxes represent N_{FCDP}. Whiskers extend to 5th and 95th percentiles, boxes encompass 25th to 75th percentiles and 50th percentiles are vertical lines. The blue box in each figure indicates the temperature of aircraft measurements.

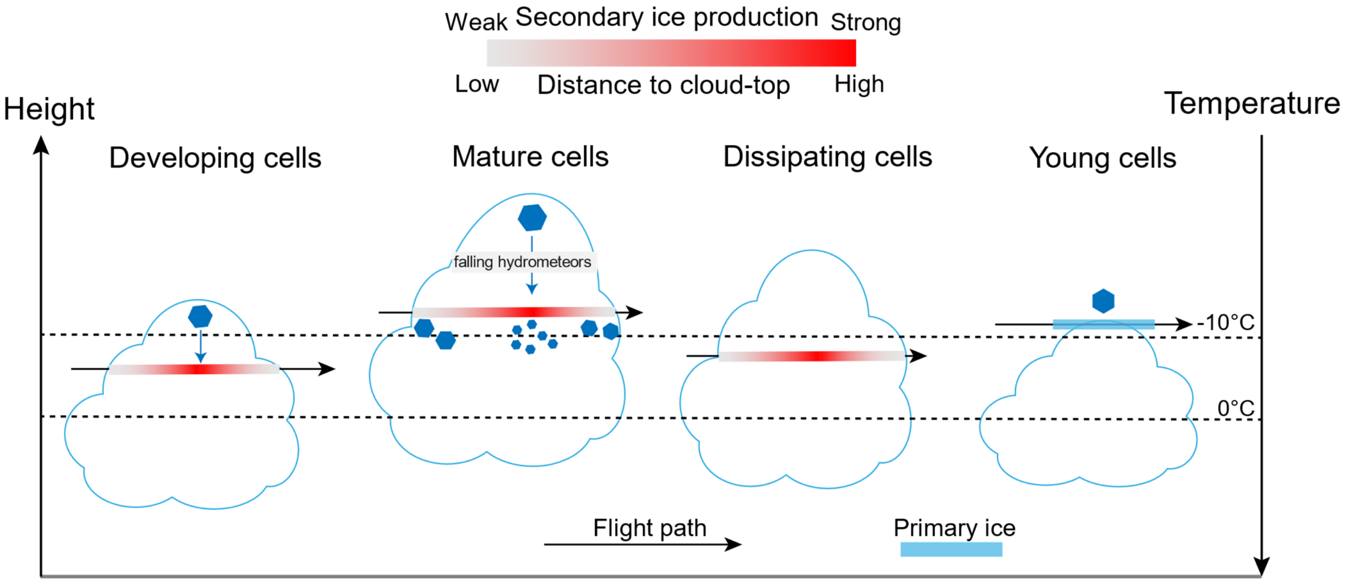

Figure 10: Schematic show of ice production at different stages of clouds.

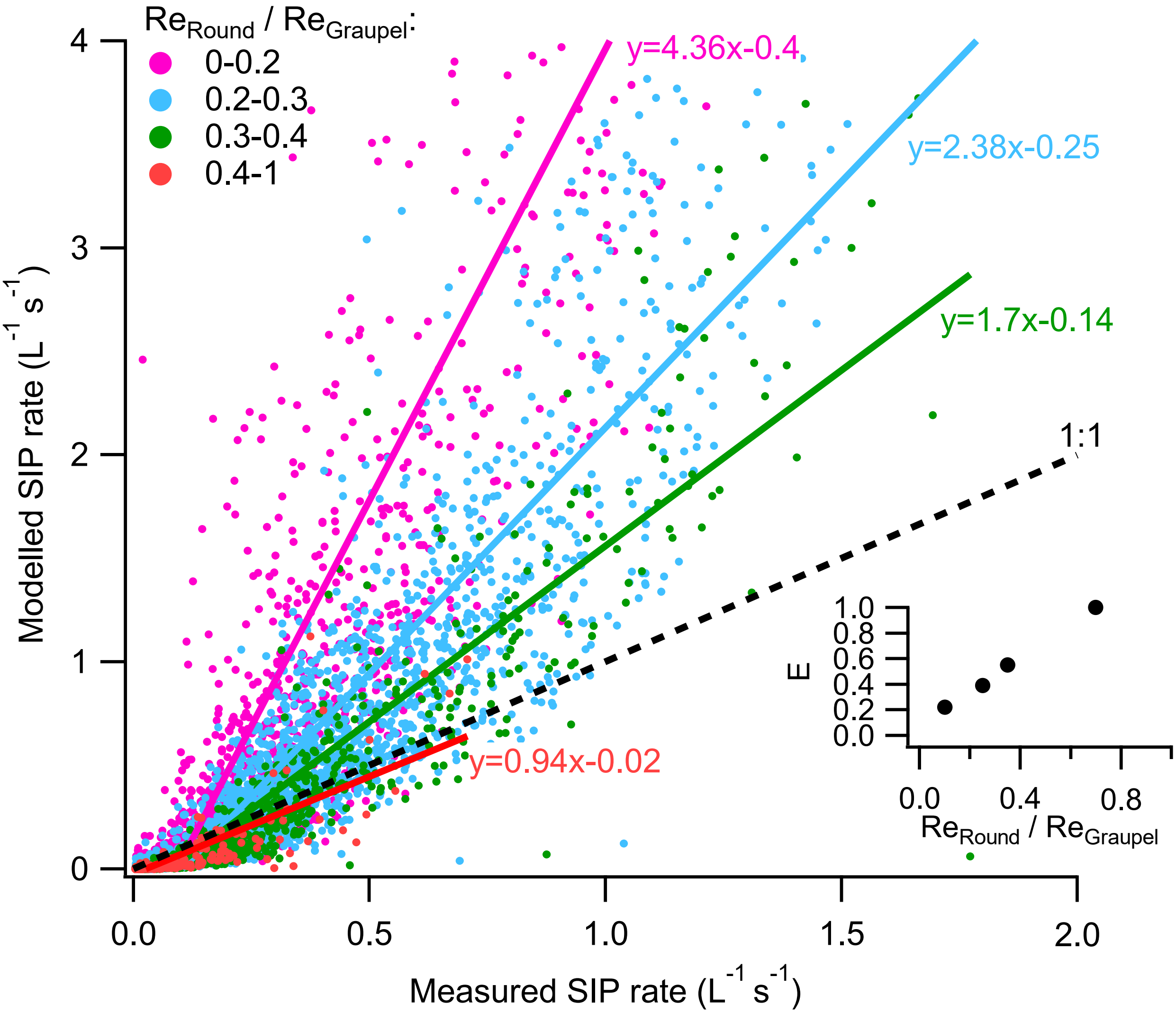

Figure 11: Measured against modelled secondary ice production (SIP) rate. The scatter plot is classified and colored by the ratio of effective radius between large droplet and graupel (Re_{Round} / $Re_{graupel}$), and each group of data points is performed least-square linear fitting. The sub-plot shows the derived collection efficiency between graupel and large droplet at different Re_{Round} / $Re_{graupel}$.